Laboratory nanoflares generated from multiple braided plasma loops

Yang Zhang[1], **Seth Pree**[1], **and Paul M. Bellan**[1]

[1]Applied Physics and Materials Science, California Institute of Technology, Pasadena, California 91125, USA.
*e-mail: yangzhan@caltech.edu

ABSTRACT

Solar flares are intense bursts of electromagnetic radiation accompanied by energetic particles and hard X-rays. They occur when magnetic flux loops erupt in the solar atmosphere. Solar observations detect energetic particles and hard X-rays but cannot reveal the generating mechanism because the particle acceleration happens at a scale smaller than the observation resolution. Thus, details of the cross-scale physics that explain the generation of energetic particles and hard X-rays remain a mystery. Here, we present observations from a laboratory experiment that simulates solar coronal loop physics. Transient, localized 7.6 keV X-ray bursts and a several kV voltage spike are observed in braided magnetic flux ropes of a 2 eV plasma when the braid strand radius is choked down to be at the kinetic scale by either magnetohydrodynamic (MHD) kink or magnetic Rayleigh-Taylor instabilities. This sequence of observations reveals a cross-scale coupling from MHD to non-MHD physics that is likely responsible for generating solar energetic particles and X-ray bursts. All the essential components of this mechanism have been separately observed in the solar corona.

Energetic particles and X-ray bursts are generated by solar flares. This generation cannot be explained by magnetohydrodynamic (MHD) physics and, instead, is presumed to depend on non-MHD physics having a characteristic length scale that is smaller than can be modeled by MHD. Because MHD is valid only for scale lengths greatly exceeding the ion skin depth which in the solar corona is about 1 to 10 m, it is likely that the scale length of the non-MHD physics that occurs when MHD breaks down is of this order. Existing solar observation technology provides significant information about energetic particles and the X-ray burst generation processes[1–5]. However, because the best resolution of solar observations is about $10^5 - 10^6$ m[6,7] and so is much coarser than the ion skin depth, many fine details cannot yet be resolved. Thus, understanding how energetic particles and X-rays are produced is a critical problem. Parker[8,9] proposed that energetic particles and X ray bursts are created by the dissipation of tiny tangential magnetic discontinuities formed from convection-caused continuous and random motion of magnetic field photospheric footpoints. He labeled the basic unit of impulsive energy release a “nanoflare" and proposed that large, X-ray producing solar flares are swarms of nanoflares each of which is too small to be resolved by existing observational methods. On the other hand, Alfvén and Carlqvist[10,11] proposed a related but somewhat different model wherein a double layer forms in a solar magnetic flux tube when the electric current density becomes very large and exceeds some threshold. The electric field associated with the double layer would accelerate particles to high energy.

We report here laboratory observations from a new configuration of the Caltech lab experiment[12–17] replicating solar coronal loops and interpret these observations in terms of a combination of the Parker nanoflare and the Alfvén/Carlqvist double-layer concepts. Specifically, transient localized 7.6 keV X-ray bursts, which we refer to as nanoflares, are observed to result from the instability of braided magnetic flux tubes containing 2 eV plasma. The phenomenological sequence leading to these bursts is determined by detailed observations using multiple interrelated diagnostics. These experimental results reveal a clear path where certain types of MHD dynamics precipitate fine-scale mechanisms, beyond the scope of MHD, that generate solar X-ray bursts and energetic particles.

Figure 1 shows the experimental set-up. Plasma-filled, current-carrying magnetic flux tubes (plasma loops) are created by a magnetized electrode structure having multiple gas nozzles that can be open or closed to produce different plasma loop configurations. The plasma loops originate from the gas nozzle positions. This arrangement enables creation of multiple braided strands. The experiment proceeds as follows: An arched 0.01 T $-$ 0.3 T vacuum magnetic field is produced on a slow (ms) timescale by electromagnets located behind the electrodes. Gas is then injected into the electrode region by valves opened on a sub-millisecond time scale. High voltage ($3-6$ kV) is applied across the electrodes on a fast (μs) timescale, breaking down the gas and creating plasma. The plasma is fully ionized, and has density $n \sim 10^{21}$ m^{-3} and temperature $\sim$ 2 to 10 eV. The plasma duration is ~ 10 μs.

Figure 2 (a) shows a sequence of high-speed photographs made by an Imacon 200 camera showing the evolution of a braided structure of multiple current-carrying plasma loops. The main capacitor bank was charged to 5 kV for this sequence and

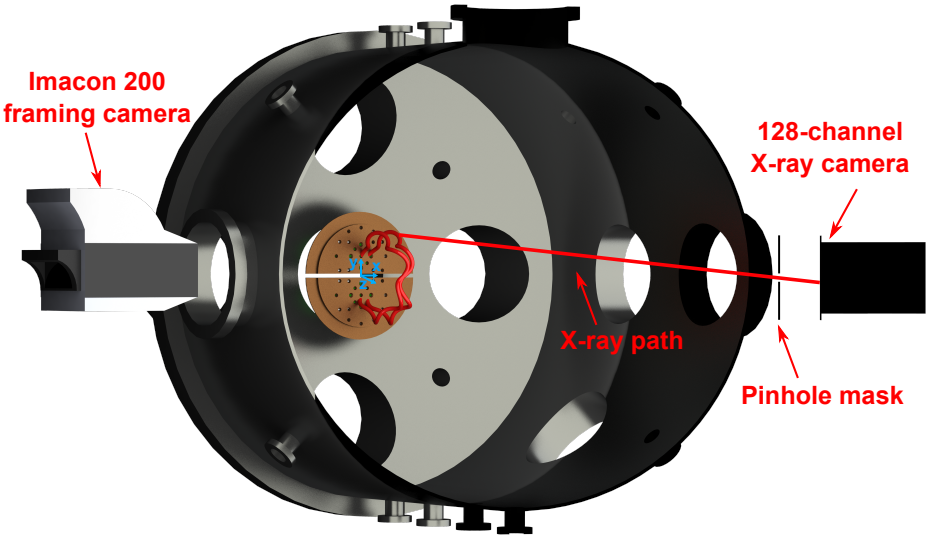

Figure 1. Experimental set-up. The electrode structure has multiple gas nozzle positions (holes), which can be open or closed and allow different configurations. This allows the creation of multiple braided strands. In this experiment, four holes are open on each electrode. The electrodes are mounted on the end dome of a 1.0-m-diameter, 1.5-m-long stainless steel vacuum chamber. Two solenoids are behind the electrodes to generate an arched magnetic field. The capacitor powering the solenoids is charged to a voltage V_b, so the bias magnetic field provided by the solenoids can be expressed as $B = \alpha V_b$, where α is a constant. Define a Cartesian coordinate system, as shown, with origin at the midpoint between electrodes, z along the vertical direction relative to electrode plane, and y along the line between the two electrode centers. Vacuum measurement of the bias field were made[13] for $V_b = 50$ V at $x = 0$ cm, $z = 3.81$ cm for two different values of y. These give $\mathbf{B} = (0,\ 0.02,\ 0.08)$T at $y = 5.08$ cm and $\mathbf{B} = (0,\ 0.04,\ 0.03)$T at $y = 7.62$ cm. Diagnostic devices include a visible-light fast framing camera, a gated linear spectroscopic array with a 1-ms time resolution, a 128-channel X-ray scintillators detector array, and a high voltage probe Tektronix P6015 measuring the voltage across the two electrodes.

the bias field coil was charged to 80 V. The braided structure consists of at least 2 strands on its upper part near the electrode (see 2.68 μs image). The hoop force resulting from the electric current flowing along the plasma loop drives a localized expanding bulge of the braided loop structure; this bulge becomes the kink instability seen in the 2.68 μs and 3.08 μs images. A kinking loop segment must lengthen as a result of the deformation of its axis but because ideal MHD instabilities such as a kink are incompressible[18], the volume of the segment must remain constant. To maintain constant volume, the radius of the segment must decrease and so the rapid lengthening of the loop segment by the kink chokes the loop radius so it becomes a thin filament and then finally breaks at 3.08-3.48 μs.

When the thin filament breaks, an X-ray burst is detected by the 128-channel X-ray detector array shown in Figure 1. A pinhole is put in front of the X-ray detector. The location of the X-ray source is determined by tracing a ray passing through the pinhole from where the ray intercepts the detector to where the ray intercepts the plasma loop. Using this procedure, the location of the source of the X-ray burst was determined to be near where the plasma loop breaks as indicated by the white box in the 3.48 and 3.88 μs frames. The uncertainty in where the X-rays originate, shown by the box size, results from the pinhole size and the signal spread on the detector array. As shown in Figure 2 (c) and (d), the X-ray burst occurs at the same time as a voltage spike measured across the plasma loop.

The detector array can alternatively be configured to measure X-ray energy; this is achieved by replacing the pinhole by multi-layer aluminum foils placed flush against the scintillators as shown in Figure 3 (a). Calibration for this energy-measuring mode is based on the X-ray intensity I through metal foil of thickness d having the dependence $I = I_0 e^{-\frac{d}{\lambda}}$ where I_0 is the incident signal and λ is a material- and energy-dependent attenuation length. The energy-dependence of the X-ray attenuation length for Aluminum (Al) is shown in Figure 3 (b)[19]. When an X-ray burst is incident on the detector configured as in Figure 3 (a), the signal is larger for detectors having fewer layers of aluminum foil. The X-ray attenuation length is determined by normalizing each group of signals to the control amplitude (channels with no foil) and then performing a linear regression on the log of the normalized signal. This measured attenuation length is then used to obtain the X-ray energy by comparing to the attenuation length plot for Al in Figure 3 (b). Each group of 32 channels was considered separately in order to reduce the impact of signal variation across the 12.8 cm width of the detector and variation in the individual PMT modules. Figure 3 (c) shows the time-dependence of the 128 channel typical X-ray raw signal using the foil layers, and Figure 3 (d) shows the X-ray

signal strength of the 128 channels with the Al filter location/strength overlayed as gray bars. Measurements from over 100 shots show that the X-ray energy ranges from 6 to 10 keV with an average of 7.6 keV.

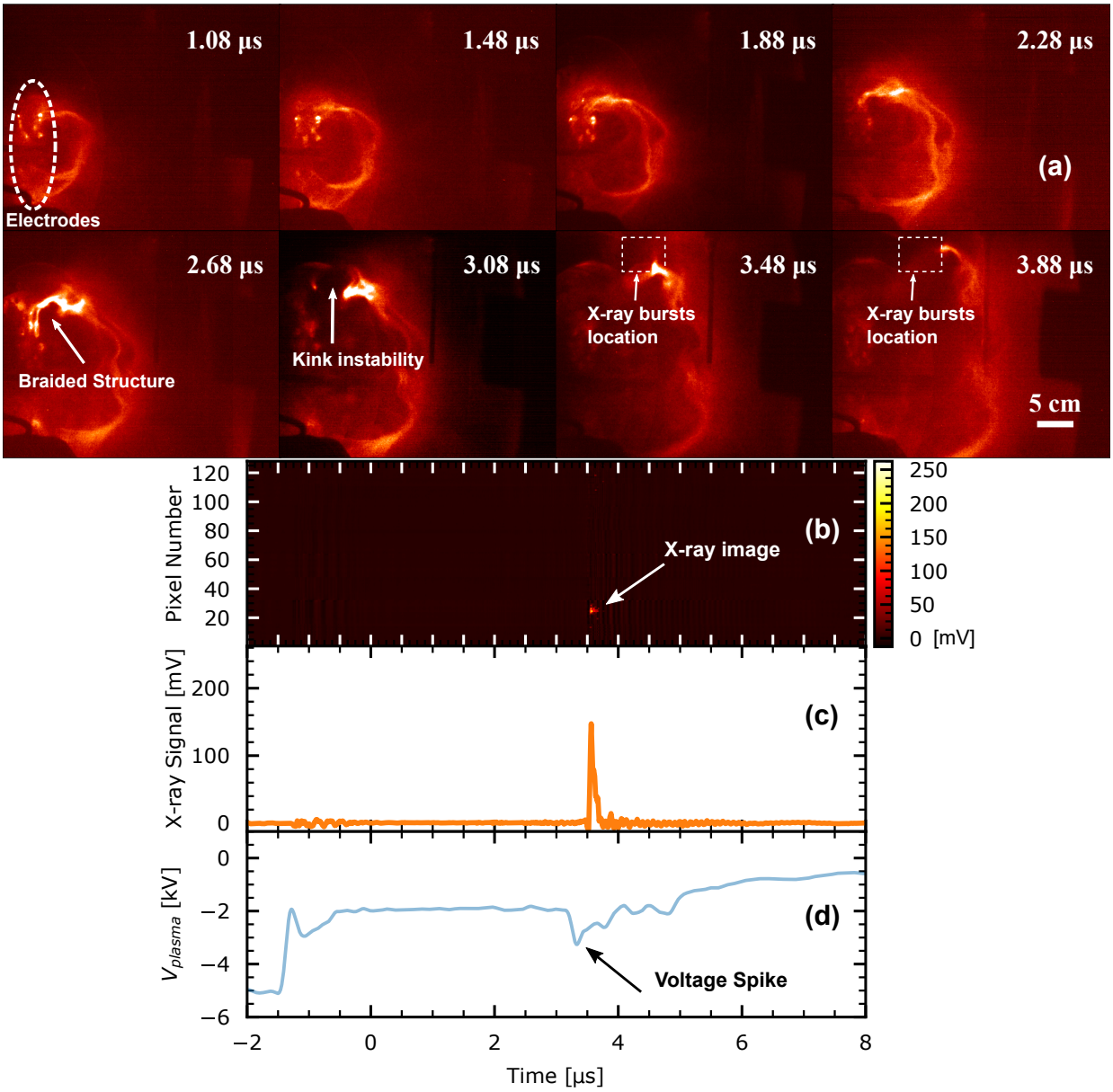

Figure 2. Time series images of experimental plasma loop evolution and X-ray and voltage measurements (a) A two-strand braided structure is observed in a time series images of hydrogen plasma loop evolution. With the expansion of the plasma loop, a kink instability occurs near the top of the loop. It chokes the strand radius down and breaks the strand at later time. A local hard X-ray burst is observed from the boxed regions in frames 7 and 8. The uncertainty in the origin of the X-rays is due to the size of the pinhole and the spread of the signal on the camera. Image is false colored. The full evolution video can be found in Supplementary Movie 1. (b) A 1-D X-ray 'movie' of the solar loop plasma. A localized X-ray source is observed from pixels 20-30 at around 3.6 μs. (c) A line out of the PMT traces is shown. (d) The voltage across the electrode. Just prior to the X-ray burst, a transient voltage spike appears across the electrodes.

The voltage spike indicates a sudden increase in the electrical resistance in series with the inductive circuit. This can be explained by two associated effects: (i) the development of a kinetic instability when the electron drift velocity $v_d = J_{axial}/ne$ associated with electric current exceeds a characteristic wave velocity such as Alfvén velocity and (ii) a geometric stretching effect. When the electron drift velocity exceeds a threshold, waves are destabilized and increase the local effective electrical resistivity[10,20]. The fastest-growing ideal MHD instabilities are incompressible[18] which means that the volume of the kinking

loop segment must remain constant during the kinking. However, when a loop segment kinks, the length l of the segment axis must increase as seen in Figure 2. The constraint that the segment is incompressible and so has constant volume requires $l\pi r^2 = const$, where r is the loop radius. The cross section πr^2 of the stretched loop segment thus decreases as the kinking stretches l; decrease of the loop cross-section means that the loop axial current density $J_{axial} = I/\pi r^2$ increases. The electron drift velocity J_{axial}/nq_e consequently increases and causes a kinetic instability that increases resistivity η. Furthermore and even without an increase in resistivity, the segment electrical resistance $R_{segment} = \eta l/\pi r^2$ will increase from the geometric stretching (increase in l/r^2). Thus, stretching not only can instigate a kinetic instability that would increase local η, but stretching also increases the resistance $R_{segment}$ simply from the change in aspect ratio. The sudden appearance of substantial resistance at the kink location has an effect equivalent to splicing a large resistor into the circuit at the location of the instability. The inductive energy of the entire circuit $LI^2/2$ could in principle be dumped into this region of increased resistivity. The large voltage jump along the length of the kinking loop strand segment resulting from LdI/dt would accelerate electrons and ions to extreme energies and the bremsstrahlung radiation of the electrons would produce X-rays.

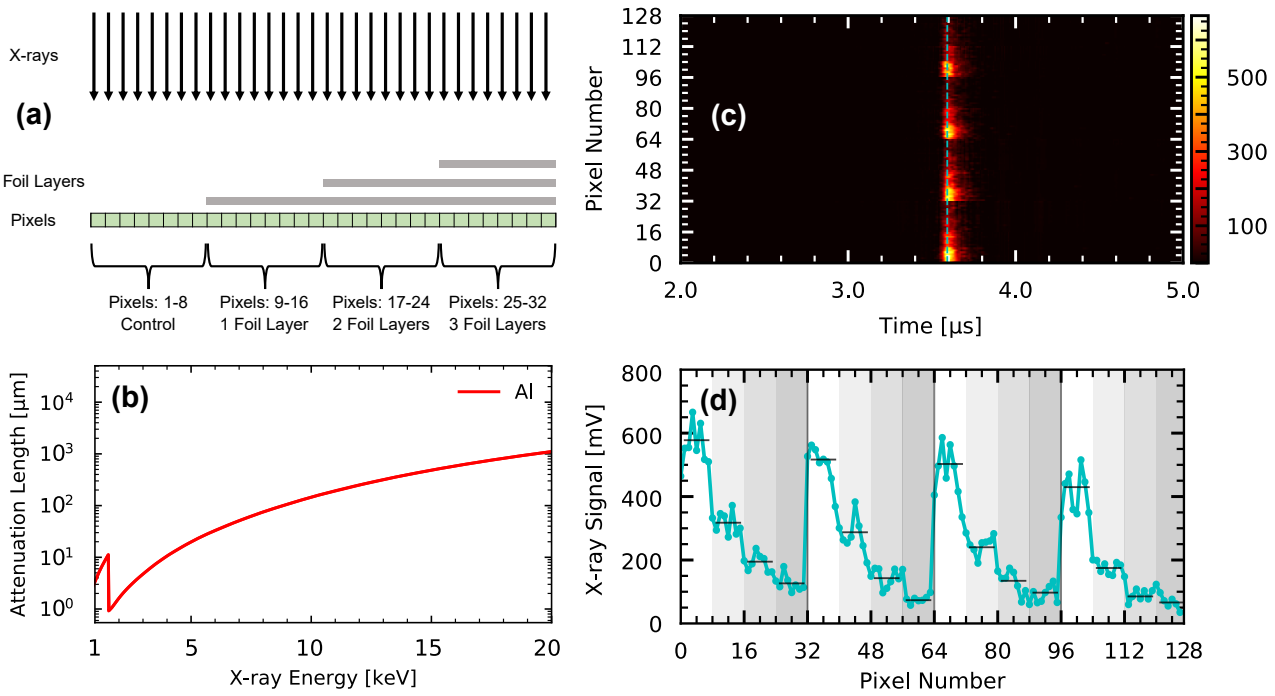

Figure 3. X-ray energy measurements. (a) A schematic diagram of the foil array placed in front of the scintillators of the X-ray detector. The foils arranged along the detector have either no additional foils (i.e. a control measurement), 36, 72, or 108 micron thick aluminum foils. (b) The NIST values of the attenuation length of X-rays of different energy through aluminum. The K-shell peak transmission window around 1.5 keV can be ignored because the polyimide window has a transmission fraction of $< 1 \times 10^{-6}$ for photon energies less than 2 keV, and the transmission fraction of the air between the window and the detector surface has a transmission fraction less than 0.01. (c) An example of the energy measurement. (d) An example line out of the measured signal. Gray bands indicate the filter placement, with darker bands indicating a thicker layer.

An electric circuit simulation verifies the idea that the voltage spike associated with the X-ray burst is induced from a sudden increase of resistivity. The LTspice circuit simulation software[21] is used to simulate the experimental circuit diagram presented in Extended Data Figure 1 (a). As there are spikes both from voltage and current measurements shown in Extended Data Figure 1 (c) and 1 (d), the resistance change should also be a spike-like peak function. To represent the cause of these spikes, as shown in Extended Data Figure 1 (b), a Gaussian time-dependent function is used to describe the sudden transient increase of resistivity. This assumed time-dependent resistance causes the circuit model to produce voltage and current spikes that nearly duplicate the experimentally measured voltage and current spikes; this is seen by comparing Extended Data Figure 1 (c) and (d) which are from the experiment with Extended Data Figure 1 (e) and (f) which are from the circuit simulation.

To see why a kinetic instability should develop when a loop strand is choked, consider the situation when the electron drift velocity is near the Alfvén velocity. The loop strand has both an axial magnetic field B_z and a local azimuthal magnetic field B_φ where the latter is associated with the current density in the strand by Ampere's law via $\mu_0 J_z = r^{-1}\partial/\partial r\left(rB_\varphi\right)$. The ratio of

electron drift velocity to the Alfvén velocity is[22]

$$\frac{v_{\rm d}}{v_A} = \frac{J_z}{ne}\frac{\sqrt{\mu_0 n m_i}}{B_z} = \sqrt{\frac{m_i}{\mu_0 n e^2}}\frac{1}{B_z r}\frac{\partial}{\partial r}\left(rB_\varphi\right) = \frac{d_i}{B_z r}\frac{\partial}{\partial r}\left(rB_\varphi\right).$$

If B_φ is of order B_z, $v_{\rm d}$ will become of order v_A if the length scale of r becomes of the order of d_i. The density of the hydrogen plasma loop is $n = 1\times10^{21}$ m^{-3} as measured from Stark broadening of the H$_\beta$ line; the ion skin depth is thus $d_i = 0.72$ cm. Before the kink instability, the diameter of a single strand is thus very close to d_i. The choking of the strand by the kink instability will consequently reduce the strand radius to be smaller than d_i. This enables a kinetic instability in the choked strand which will increase the resistivity in the strand. This resistivity increase together with the increase in strand segment l/r^2 increases the local electrical resistance.

A magnetic Rayleigh Taylor instability (MRTI, or Kruskal–Schwarzschild instability[23]) can also occur in the plasma loop as shown in Extended Data Figure 2 and the MRTI works similarly to the kink instability to choke the plasma strand radius down to the kinetic scale.

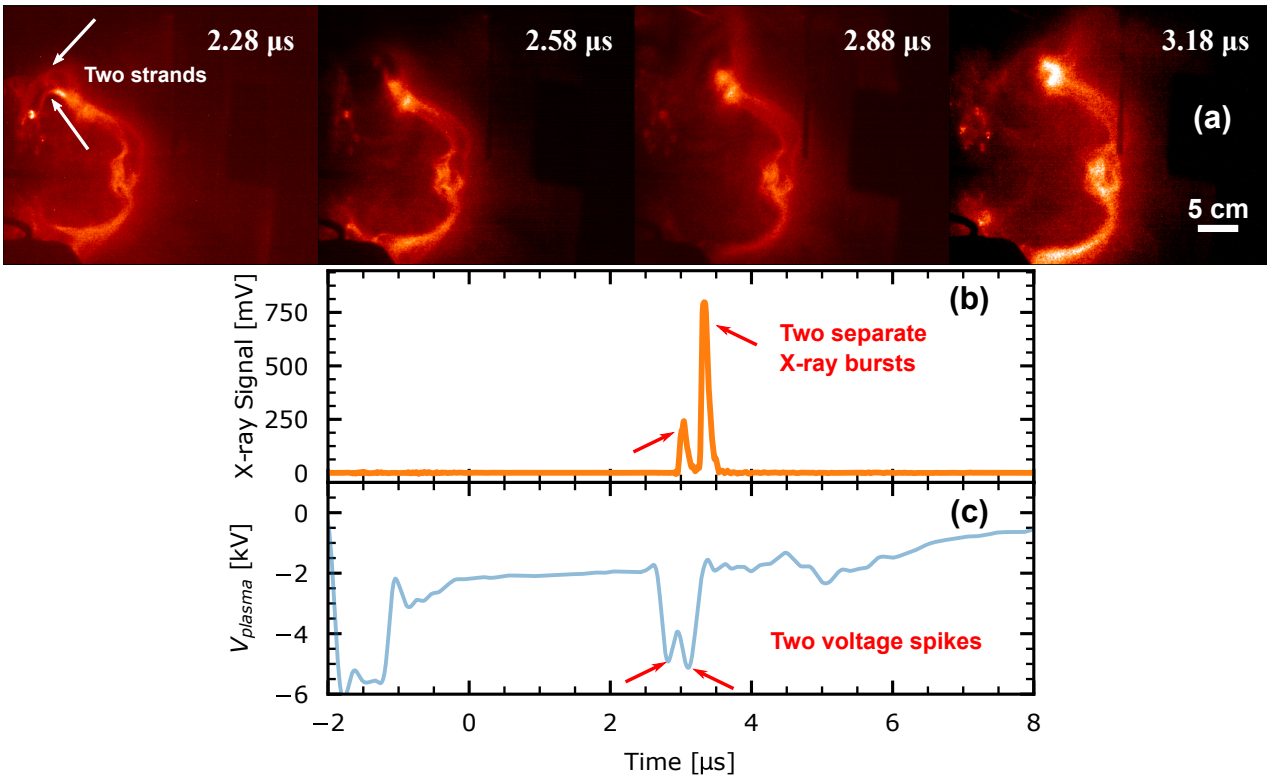

Figure 4. Two experimental nanoflare events. (a) The image shows a braided structure of 2 strands in a time series images of hydrogen plasma loop evolution. (b) X-ray traces are shown. They show two separate X-ray bursts. (c) The voltage across the electrodes. Just prior two separate X-ray bursts, two separate voltage spikes are measured.

We define a single X-ray burst as a laboratory nanoflare and sometimes observe multiple nanoflares. Figure 4 (a) shows an experiment shot where the plasma loop is composed of two separate strands. Two separate X-ray bursts are detected in Figure 4 (b) and two ~ 3 kV spikes were measured as shown in Figure 4 (c). These bursts and associated voltage spikes are presumed to be generated as each of the two strands went unstable and broke via the mechanism described above. Three laboratory nanoflares in one shot have also been observed.

These experimental results suggest a multi-scale instability sequence wherein solar loops initially governed by ideal MHD dynamics kink which then chokes the current channel and trigger kinetic instability which then instigates opening-switch-like processes that cause solar X-ray bursts.

The MHD behavior reported here can be scaled to the many other situations governed by MHD because MHD has no intrinsic length scale. MHD scaling[24] allows for three free parameters: a_1, a_2 , a_3, following invariant relations: $\frac{L_0}{a_1} \to L'$, $\frac{\rho_0}{a_2} \to \rho'$, $\frac{B_0}{\sqrt{a_3}} \to B'$, $\frac{P_0}{a_3} \to P'$, $\frac{1}{a_1}\sqrt{\frac{a_3}{a_2}}t \to t'$, $\sqrt{\frac{a_2}{a_3}}v_0 \to v'$ to transform a scale to another scale having the same plasma beta.

This transformation gives a one-to-one correspondence between systems, allowing laboratory experimental plasmas to be scaled to equivalent systems in space plasmas. Table 1 shows characteristic parameters of the experiment, the solar corona and the experiment scaled to the solar corona using $a_1 = 10^{-8}$, $a_2 = 1 \times 10^5$, $a_3 = 9 \times 10^2$. The scaled characteristic parameters have magnitudes similar to that of the solar corona.

Table 1 Experimental plasma parameters and scaling to the solar corona

	Experiment	Scaled Experiment	Solar Corona
Characteristic length L (m)	0.05	5×10^6	5×10^6
Characteristic time t (s)	10^{-6}	10	10
Magnetic field B (G)	3000	100	100
Mass density ρ(kg $\cdot$ m^{-3})	1.7×10^{-6}	1.7×10^{-11}	1.7×10^{-11}
Pressure P(Pa)	800	0.89	0.32
Alfven velocity v_A(m $\cdot$ s^{-1})	2.1×10^5	2.2×10^6	2.2×10^6
Plasma beta β	0.02	0.02	0.01
Lundquist number S	200		2×10^{13}
Ion skin depth d_i(m)	0.007		2

Table 1. Plasma parameters of Caltech experiment and scaling to solar corona. Typical values of the experiment (left column) are scaled according to the MHD scaling described in the text. The scaled values (center column) are in good agreement with approximate values for the solar corona (right column). This close correspondence indicates magnetohydrodynamic similarity between the two systems and the relevance of the experimental parameter regime to that of the solar corona. The experiment plasma has a density 10^{21} m^{-3} and a temperature 5 eV. The solar corona has a density 10^{17} m^{-3} and a temperature 200 eV[25].

A critical distinction between the lab and solar situations is that the initial state of the lab experiment is much closer to kinetic instability than at first consideration would apparently be the case for the solar situation. The initial current channel radius in the experiment is around d_i so that the kink instability does not have to choke the current channel cross-section very much. In contrast, the nominal radius of a solar coronal loop is of order of 10^6 m whereas the ion skin depth for nominal solar corona densities is of order of 1 to 10 m. The length of the solar loop would have to increase by an unrealistically large amount to choke the 10^6 m radius to be of the order of 10 m. The solar situation could nevertheless develop a kinetic instability on realizing that a solar coronal flux rope is not monolithic but instead is a fractal braid of successively smaller braided filamentary flux ropes, i.e., strands. The finest strand would be close to ion skin depth, i.e., $\sim$10 m to $\sim$100 m. Because of this fractal braiding, an MHD instability only has to choke an individual finest MHD-governed strand by a small factor to instigate kinetic instability.

A finest scale structure of 10 m is consistent with the required magnetic field diffusion time. Solar loops are stable for time scales of hours and have an internal axial current providing the $\mathbf{J} \times \mathbf{B}$ inward force that balances outward forces from the pressure gradient in the direction of the loop radius. The time for this current to become distributed over the loop cross section is the magnetic field diffusion time $\tau_r = \mu_0 r^2/\eta$, where r is the radius and η is the resistivity. The temperature of a solar corona loop is $T = 200$ eV so Spitzer resistivity gives $\eta = 7 \times 10^{-7}\ \Omega \cdot$m. Thus, a 3600 s diffusion time corresponds to a 45 m radius. If the solar corona loop were a monolithic structure (like a solid copper wire) having a 10^6 m radius rather than being constituted by fractal strands, the magnetic field diffusion time would be 6×10^4 yr which is orders of magnitude greater than observed characteristic solar magnetic field evolution time scales. This implies that a fractal structure is necessary for a solar corona loop to have a distributed current. Filamentary decomposition of a flux rope is analogous to Litz wire[26], which is composed of braided tiny, insulated wire strands. This structure can enhance current penetration compared with a single monolithic conductor and so links more interior flux and increases the inductance[27].

The essential components of this mechanism have been separately observed in nature. Solar observations imply that coronal loops are composed of braided flux ropes because, as imaging resolution has increased over the years, each improvement in resolution has revealed finer-scale structure[25]. Braided loop structures have commonly been observed on the Sun, for example by the High-resolution Corona Imager[1]. Fast-growing ideal MHD instabilities such as the kink instability and the magnetic RTI are common in solar loop structures[28,29]. Previous study has shown that a large current flows through the solar loop and the current disruption from LdI/dt can generate voltage spikes up to 10^6 kV[10]. Fleishman et al. measured the rapid magnetic field decay in a solar flare region, which implies a strong inductive electric field[3,5] with associated voltage spike $V = -d\phi/dt = -LdI/dt$ where the magnetic flux is $\phi = \int \mathbf{B} \cdot d\mathbf{S} = LI$ and I is the electric current. Nanoflares have also been

observed[2,4].

A specific highly-relevant example is the kink-driven solar flare observed in active region NOAA 11163 on February 24, 2011[30] which had an evolution very similar to what was observed in the Caltech lab experiment. Compared with the Caltech experiment, it has a bigger length scale (20 Mm) but a slower time scale (10 s). The MHD behavior of both situations can be scaled and compared using Table 1. Figure 5 (a-c) presents high-resolution observations of this kink-driven solar flare as observed by the Solar Dynamics Observatory (SDO)/Atmospheric Imaging Assembly (AIA)[6] while Figure 5 (d-f) show the comparable situation in the Caltech lab experiment. In both the active region and the lab experiment, a kink instability developed on a loop segment and in both cases the axial stretching produced by the kink chokes the radius of the segment and then the choked segment breaks. Figure 5 (g) shows the hard X-ray signal from RHESSI[31] for the solar kink-driven instability and Figure 5 (h) shows the X-ray signal from the lab experiment.

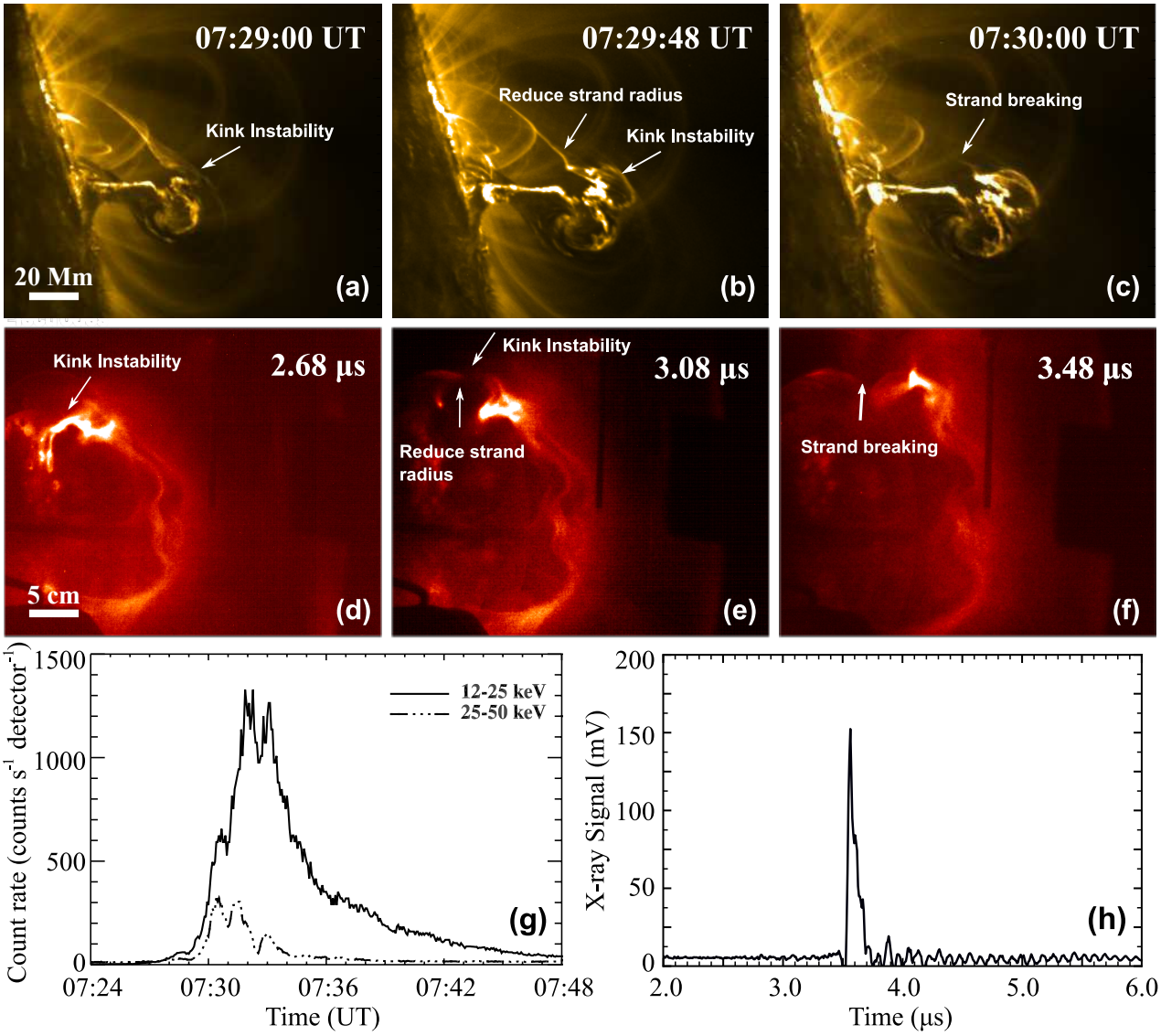

Figure 5. Comparison between solar observation and experimental observation. (a-c) SDO/AIA 171 (T∼0.6 MK) Å EUV images showing the development of kink instability, associated CME, and flare which occurred in active region NOAA 11163 on 2011 February 24. (d-f) Experimental images showing the similar process as (a-c). (g) RHESSI hard X-ray flux profiles (12–25 and 25–50 keV). Hard X-ray bursts are observed during the process. (h) hard X-ray signals observed in the experiment associated with this process. (a, b, c, g) are reproduced by permission of the AAS[30].

It is thus reasonable to propose the following path for how solar eruptions create energetic particles and X-rays: (i) A solar flux rope is conjectured to be a braid of a very large number of fine-scale flux ropes with the finest scale being somewhat larger

than d_i; (ii) Electric current flows along the flux rope and the corresponding hoop force causes a segment or segments of the flux rope to bow out; (iii) Each strand then develops a fast-growing MHD instability, such as the kink instability or magnetic RTI which then chokes the strand down to a critical scale at which time kinetic instabilities develop and, together with the stretching of the length of the unstable strand, increase the resistance of the choked segment; (iv) This increase in resistance corresponds to an opening switch so the inductive energy of the entire circuit would be dumped into this region of increased resistance; (v) A high voltage drop resulting from LdI/dt would accelerate electrons and ions to extreme energies and the bremsstrahlung radiation of the electrons would produce X-rays.

The particle acceleration mechanism proposed here is also likely relevant to space and astrophysics regimes. A similar voltage spike double layer structure has been observed in Earth's plasma sheet and identified as a cause for particle accelerations[32].

References

1. Cirtain, J. W. *et al.* Energy release in the solar corona from spatially resolved magnetic braids. *Nature* **493**, 501–503 (2013).
2. Testa, P. *et al.* Evidence of nonthermal particles in coronal loops heated impulsively by nanoflares. *Science* **346**, 1255724 (2014).
3. Fleishman, G. D. *et al.* Decay of the coronal magnetic field can release sufficient energy to power a solar flare. *Science* **367**, 278–280 (2020).
4. Bahauddin, S. M., Bradshaw, S. J. & Winebarger, A. R. The origin of reconnection-mediated transient brightenings in the solar transition region. *Nat. Astron.* **5**, 237–245 (2021).
5. Fleishman, G. D., Nita, G. M., Chen, B., Yu, S. & Gary, D. E. Solar flare accelerates nearly all electrons in a large coronal volume. *Nature* **6**, 674–677 (2022).
6. Lemen, J. R. *et al.* The atmospheric imaging assembly (AIA) on the solar dynamics observatory (SDO). In *The solar dynamics observatory*, 17–40 (Springer, 2011).
7. Kobayashi, K. *et al.* The high-resolution coronal imager (Hi-C). *Sol. Phys.* **289**, 4393–4412 (2014).
8. Parker, E. Magnetic neutral sheets in evolving fields. I - General theory. *The Astrophys. J.* **264**, 635–647 (1983).
9. Parker, E. Nanoflares and the solar X-ray corona. *The Astrophys. J.* **330**, 474–479 (1988).
10. Alfvén, H. & Carlqvist, P. Currents in the solar atmosphere and a theory of solar flares. *Sol. Phys.* **1**, 220–228 (1967).
11. Carlqvist, P. Current limitation and solar flares. *Sol. Phys.* **7**, 377–392 (1969).
12. Stenson, E. V. & Bellan, P. Magnetically driven flows in arched plasma structures. *Phys. Rev. Lett.* **109**, 075001 (2012).
13. Ha, B. N. & Bellan, P. M. Laboratory demonstration of slow rise to fast acceleration of arched magnetic flux ropes. *Geophys. Res. Lett.* **43**, 9390–9396 (2016).
14. Wongwaitayakornkul, P., Haw, M. A., Li, H., Li, S. & Bellan, P. M. Apex dips of experimental flux ropes: Helix or cusp? *The Astrophys. J.* **848**, 89 (2017).
15. Haw, M. A., Wongwaitayakornkul, P., Li, H. & Bellan, P. M. Reverse current model for coronal mass ejection cavity formation. *The Astrophys. J. Lett.* **862**, L15 (2018).
16. Wongwaitayakornkul, P., Haw, M. A., Li, H. & Bellan, P. M. Magnetically induced current piston for generating extreme-ultraviolet fronts in the solar corona. *The Astrophys. J.* **874**, 137 (2019).
17. Zhang, Y., Wongwaitayakornkul, P. & Bellan, P. M. Magnetic Rayleigh–Taylor instability in an experiment simulating a solar loop. *The Astrophys. J. Lett.* **889**, L32 (2020).
18. Newcomb, W. A. Hydromagnetic stability of a diffuse linear pinch. *Annals Phys.* **10**, 232–267 (1960).
19. Henke, B. L., Gullikson, E. M. & Davis, J. C. X-ray interactions: photoabsorption, scattering, transmission, and reflection at E= 50-30,000 eV, Z= 1-92. *At. data nuclear data tables* **54**, 181–342 (1993).
20. Buneman, O. Dissipation of currents in ionized media. *Phys. Rev.* **115**, 503–517 (1959).
21. Engelhardt, M. LTspice owned by Analog Devices Inc.; software available at https://www.analog.com/en/design-center/design-tools-and-calculators/ltspice-simulator.html .
22. Moser, A. L. & Bellan, P. M. Magnetic reconnection from a multiscale instability cascade. *Nature* **482**, 379–381 (2012).

23. Kruskal, M. D. & Schwarzschild, M. Some instabilities of a completely ionized plasma. *Proc. Royal Soc. London. Ser. A. Math. Phys. Sci.* **223**, 348–360 (1954).

24. Ryutov, D., Drake, R. & Remington, B. Criteria for scaled laboratory simulations of astrophysical MHD phenomena. *The Astrophys. J. Suppl. Ser.* **127**, 465 (2000).

25. Aschwanden, M. *Physics of the solar corona: an introduction with problems and solutions* (Springer Science & Business Media, 2006).

26. Sullivan, C. R. & Zhang, R. Y. Simplified design method for litz wire. In *2014 IEEE Applied Power Electronics Conference and Exposition-APEC 2014*, 2667–2674 (2014).

27. Stix, T. H. Magnetic braiding in a toroidal plasma. *Phys. Rev. Lett.* **30**, 833 (1973).

28. Srivastava, A., Zaqarashvili, T., Kumar, P. & Khodachenko, M. Observation of kink instability during small B5. 0 solar flare on 2007 june 4. *The Astrophys. J.* **715**, 292 (2010).

29. Hillier, A. The magnetic Rayleigh–Taylor instability in solar prominences. *Rev. Mod. Plasma Phys.* **2**, 1 (2018).

30. Kumar, P., Cho, K.-S., Bong, S.-C., Park, S.-H. & Kim, Y. Initiation of coronal mass ejection and associated flare caused by helical kink instability observed by SDO/AIA. *The Astrophys. J.* **746**, 67 (2012).

31. Lin, R. P. *et al.* The Reuven Ramaty high-energy solar spectroscopic imager (RHESSI). In *The Reuven Ramaty High-Energy Solar Spectroscopic Imager (RHESSI)*, 3–32 (Springer, 2003).

32. Ergun, R. *et al.* Observations of double layers in earth's plasma sheet. *Phys. Rev. Lett.* **102**, 155002 (2009).

Acknowledgements

This material is based upon work supported by NSF Award Numbers 1914599 and 2105492. The X-ray detector used in this work was developed with support from USDOE ARPA-E Grant DE-AR0001159.

Author contributions

Y.Z. designed the braided loop experiment from suggestions and guidance of P.M.B. S.P. built the X-ray camera from suggestions and guidance of P.M.B. Y.Z. and S.P. performed the experiment. The interpretation of the results was done jointly by all authors. Y.Z. drafted the manuscript. All authors revised the manuscript together.

Data availability

Experimental data were generated from the Caltech Solar Loop Experiment. They are available from the corresponding author upon reasonable request.

Code availability

Information about LTspice circuit simulation software is available at https://www.analog.com/en/design-center/design-tools-and-calculators/ltspice-simulator.html. The circuit simulation code is available from the corresponding author upon reasonable request.

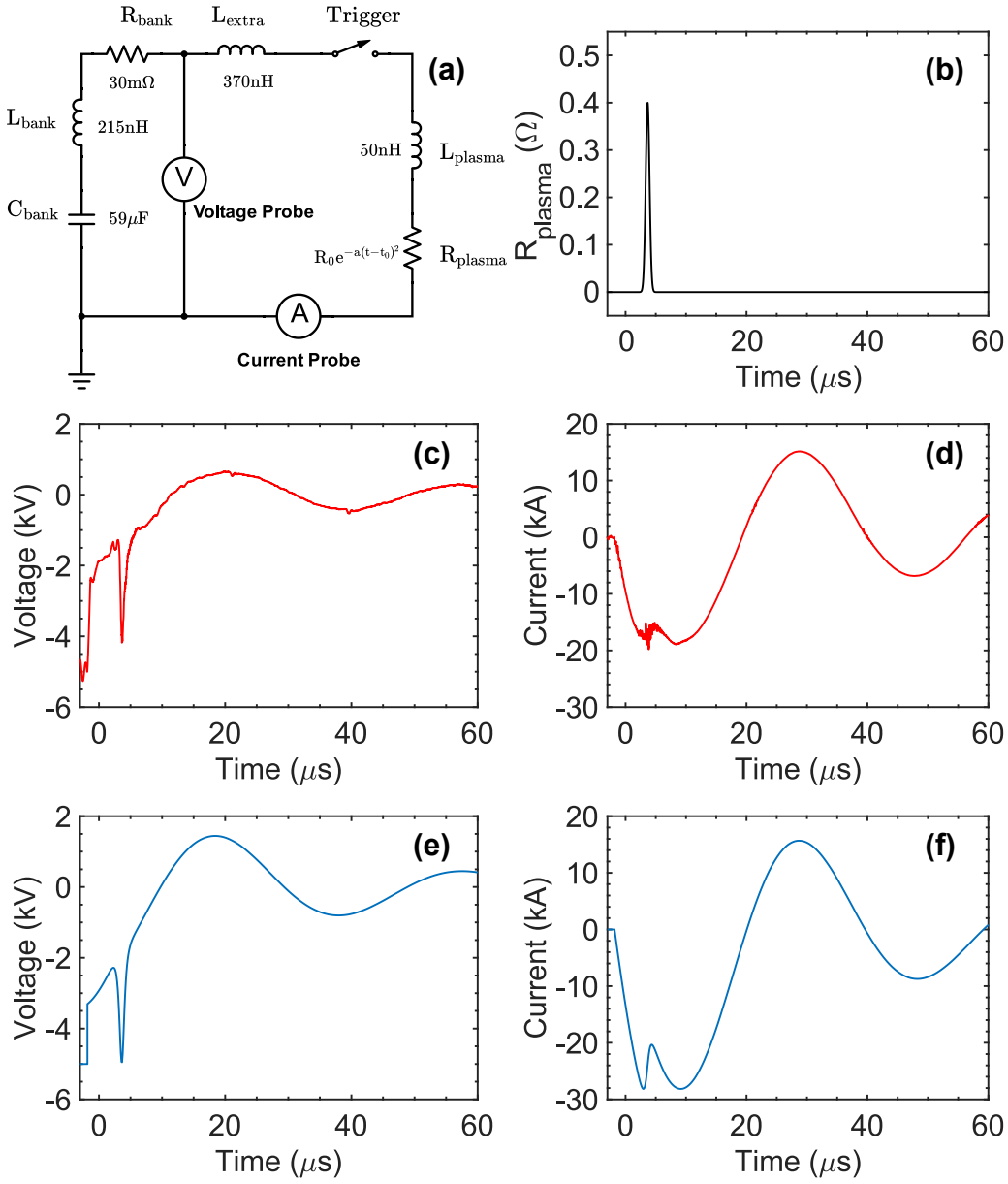

Extended Data Figure 1. Solar loop experiment circuit simulation. (a) Experiment circuit diagram. The plasma part of the circuit is represented as an inductor and a time-dependent resistor. The plasma inductance is assumed to be 50 nH, which is obtained by simplifying the plasma loop as a half circle loop of wire with 5 cm loop major radius and 1 cm minor (wire) radius. The voltage and current spikes are both peak functions, so the corresponding resistance change is presumed to be also a peak function. We use Gaussian function $R_{plasma} = R_0 \exp(-a(t-t_0)^2)$ to represent the transient change of the plasma resistance where R_0 is the peak resistance value, and t_0 is the resistance peak time, and a is related to the full width at half maximum (FWHM). They are chosen according to the relative voltage spike amplitude, voltage peak time and the voltage spike FWHM. In the simulation, $R_0 = 0.4\ \Omega$, $t_0 = 3.65\ \mu s$ and $a = 5\ \mu s^{-2}$ are used. The corresponding plasma resistance is plotted in (b). (c, d) Voltage and current measurement from experiment Shot # 9258. As shown in (a), the voltage measured in (c) is the voltage across the plasma part and an extra inductor. We also measured the voltage across the plasma part by connecting two voltage probes directly to the top electrode and bottom electrode and then subtracting the two voltages. The voltage trace across the plasma is similar but has a several kV larger voltage spike compared with (c). (e, f) Voltage and current curves from the simulation. Voltage and current spikes similar to the experimentally observed spikes are reproduced by the transient resistance increase.

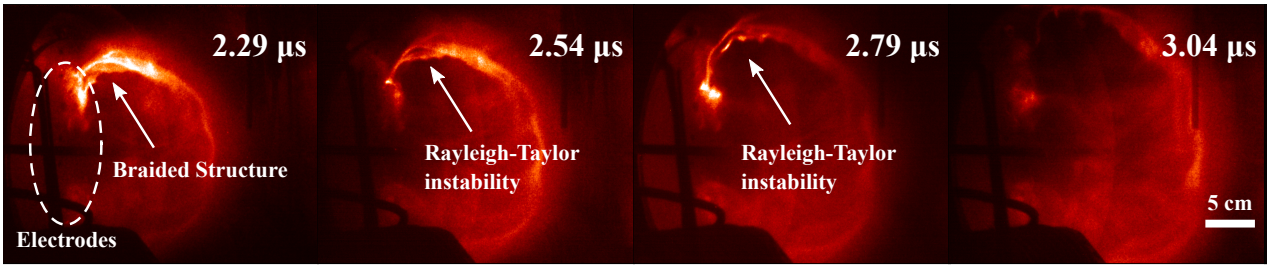

Extended Data Figure 2. Magnetic Rayleigh Taylor instability observation. A four-strand braided structure is shown in time series images of hydrogen plasma loop evolution. With the expansion of the plasma loop, a magnetic Rayleigh Taylor instability occurs on the loop and plays the same role as a kink instability to choke the strand radius down and break the strand at later time. The full evolution video can be found in Supplementary Movie 2.